scientific reports

Check for updates

OPEN

Cluster analysis reveals increasing plume-like magmatism during progressive rifting in Afar (Ethiopia)

Gianmaria Tortelli[1✉], Pierluigi Crescenzi[2], Carolina Pagli[3], Anna Gioncada[3], Derek Keir[1,4] & Linda Pagli[5]

Reconstructing chemical variations of magma during rifting is challenging due to the heterogeneous mantle sources of the melt and different evolution pathways that magma potentially takes. Therefore, how and when the magma generation process evolves to that typical of an oceanic ridge (MORB-like composition) is still unclear. The Afar depression is an ideal place for studying magma changes during rift evolution, with North Afar close to breakup and older rift products preserved across the region. To investigate magma sources, we applied clustering analyses to a vast geochemical dataset of more than 1000 samples from the Afar rift. Combinations of different clustering methods (K-means and hierarchical) and assessment of correlation between features (Pearson coefficient) show that both trace element and isotope clustering group the North Afar samples, identifying a mantle source containing residual MREE-bearing minerals and an enriched mantle component. This suggests that North Afar, where the rift is closest to breakup, has a stronger influence of the Afar plume and more extensive partial melting of metasomatized lithosphere than the rest of Afar. We show that geochemical variations during rifting do not always follow a progressive transition toward a MORB-like composition but, instead, plume-like magmatism can increase until the most advanced stages of rifting (i.e., North Afar), potentially because the mantle plume is focused towards regions of thinnest lithosphere.

In magma-rich continental rifts, the chemical composition of the erupted magma can vary significantly due to a complex range of processes including the mantle sources, degree of partial melting, fractional crystallisation and crustal assimilation[1–5]. Geochemical studies are widely used to discriminate between different magmatic processes and to constrain the mantle reservoirs sourced during partial melting[6]. During progressive rifting through to continental breakup and the initiation of seafloor spreading, magmas may derive from diverse and heterogeneous mantle reservoirs, whose individual contributions to magma genesis can change in space and time and are therefore difficult to unravel[1,3,7–11]. Some studies have pointed towards an overall increase of depleted mantle melting through time[3,12]. However, an increase of a mantle plume component with decreasing age has also been observed[13–15]. In addition melting of metasomatized portions of the lithospheric mantle can influence melt composition[5,14,16–18], as these portions may retain the chemical signature of the metasomatic agent, such as a mantle plume, further complicating the identification of individual mantle source contributions.

Geochemical studies are crucial to resolve these variations and understand how mantle melting occurs during rift evolution. However, conventional approaches rely on visual interpretations, mostly of binary and ternary classification diagrams, which are limited in dimensionality[19,20]. Moreover, the geochemical approach is often based on a-priori distinction of the rocks based on sample location and/or age. In contrast, unsupervised machine learning clustering analysis allows to statistically group samples of large, multivariate datasets without any a-priori distinction, therefore representing a powerful tool to classify geochemical data[21–24]. We apply this approach to a comprehensive geochemical database from the Afar rift to investigate how the contribution of the mantle reservoirs change during the evolution of the rift.

Rifting in Afar initiated around the same time as the main phase of Ethiopian-Yemen Flood Basalt eruption at ~ 31–29 Ma[25], and the magmatic record of rift evolution is currently exposed within the rift depression (Fig. 1). The oldest erupted products are the silicic Mabla series (20–10 Ma) and the mainly mafic Dalha series (10–4 Ma), outcropping along the Afar margins[26] (Fig. 1). The central area of the depression is instead dominated by the widespread, thick (up to 1 km) and mostly mafic Lower Stratoid series (LS; 4.9–2.6 Ma) in South Afar and

[1]Department of Earth Science, University of Florence, Florence, Italy. [2]Gran Sasso Science Institute, L'Aquila, Italy. [3]Department of Earth Science, University of Pisa, Pisa, Italy. [4]School of Ocean and Earth Science, University of Southampton, Southampton, UK. [5]Department of Computer Science, University of Pisa, Pisa, Italy. ✉email: gianmaria.tortelli@unifi.it

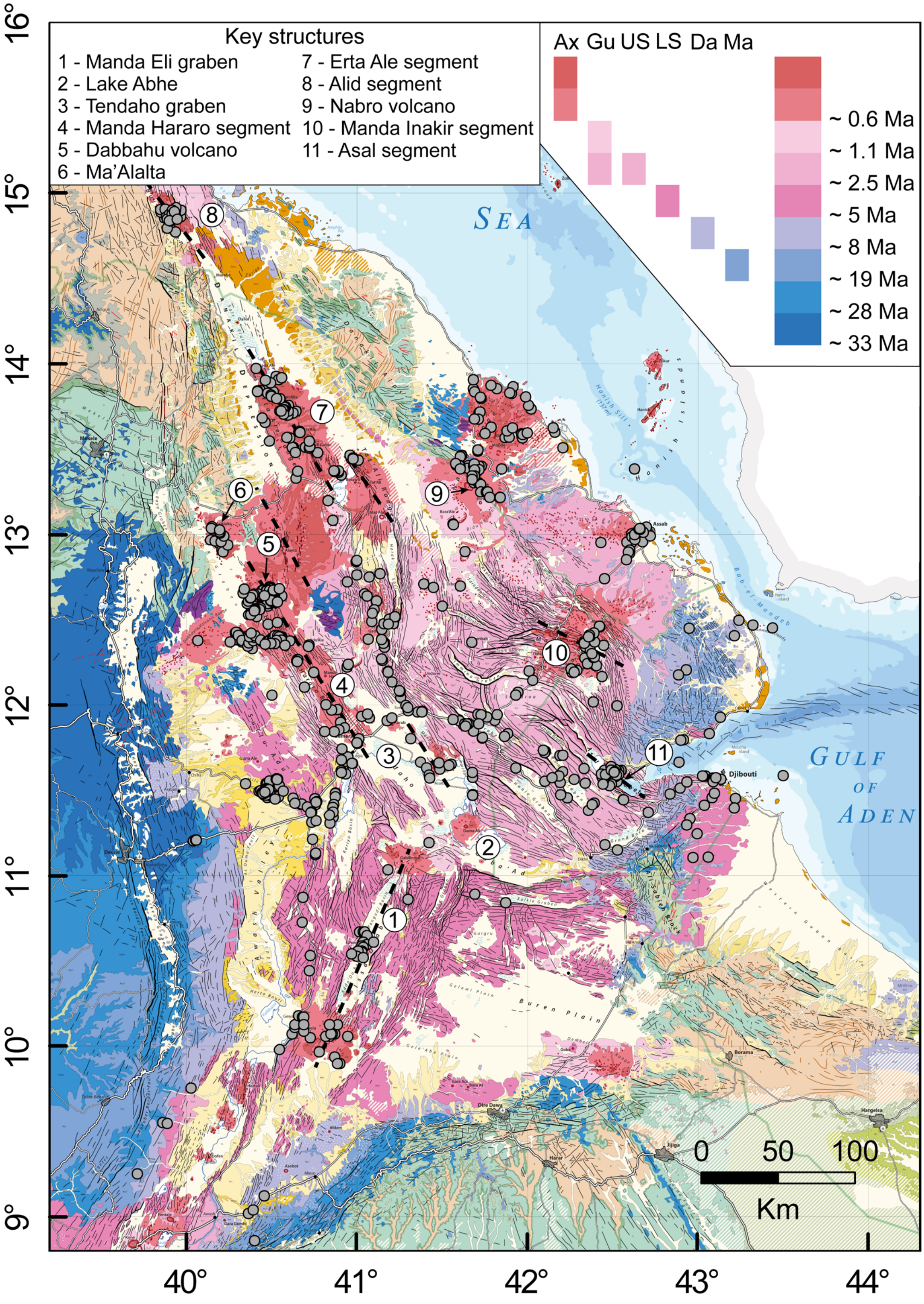

Fig. 1. Sampling and geological map. Geological map of the Afar Depression, modified from Rime et al.[57]. All samples used in this study are presented, along with the key structures of the Afar region and the associated volcanic deposits. Ax – Axial Series; Gu – Gulf Series; US – Upper Stratoid Series; LS – Lower Stratoid Series; Da – Dalha Series; Ma – Mabla Series. The black dashed lines identify the Afar main magmatic segments. This figure was created using ArcGIS Pro 3.4.0 (https://www.esri.com/en-us/home).

the Upper Stratoid series (US; 2.9–0.9 Ma) in Central Afar[27,28]. This is followed by eruptions of the Gulf series (Gu; 2.8–0.3 Ma) marking the formation of the magmatic segments, currently erupting the Axial series[27,29,30] (Ax; <0.7 Ma; e.g., Manda Hararo, Asal, Erta Ale).

The existence of a mantle plume in the East African Rift System is suggested by the elevated ^{3}He/^{4}He ratios in magmas[7] and the anomalously high mantle temperatures[27,31] (1400–1500 °C) both pointing to mantle material rising from a thermal upwelling. Rooney[9] pointed out that the magmatism is generated by the rising Afar Plume (AP), similar in composition to the oceanic basalts 'common' reservoir[32], variably mixing with the shallower Depleted MORB Mantle (DMM) and Pan African lithosphere (PAL) reservoirs[4,26–28]. The PAL records a complex history, shaped by the assembly of terranes during the Pan-African orogeny. Subsequently, ancient subduction-related metasomatism (imparting HIMU-like signature) and Cenozoic plume-driven metasomatism (imparting AP-like signature), modified the subcontinental lithosphere, adding complexity to the three-end-member model (i.e., AP, DMM, and PAL). The magmatism of Mabla, Dalha, LS, US and Gu reveal similar involvement of the three reservoirs[26,27]. Mabla and Dalha are distinguished by evidence of crustal contamination (i.e., ^{87}Sr/^{86}Sr and ^{143}Nd/^{144}Nd)[26] while the US are distinct from LS and Gu due to their deeper melting depth (i.e., Dy/Yb)[28]. Axial volcanism shows instead greater isotopic variability compared to the older volcanic products (e.g., ^{143}Nd/^{144}Nd and ^{206}Pb/^{204}Pb). This variability is attributed to differences in the PAL and Afar Plume contributions, the intrinsic heterogeneity of the Afar Plume and/or variations in the lithospheric composition due to Afar plume-induced metasomatism[11,13,26].

Although the magmatic activity of a new formed ocean will eventually be fed by a Depleted MORB-like mantle source[33,34], unravelling chemical variations to determine how and when the mantle reservoirs changes during rifting remains challenging[12,14,15]. In this work we use cluster analysis on a large geochemical dataset from the entire Afar triple junction (Ethiopia) to understand changes in magma genesis and evolution during rifting. By means of cluster analysis we were able to identify the variation in the depth of partial melting within Central and Southern Afar and reveal an increase of metasome melting for Northern Afar with respect to Central-Southern Afar. Furthermore, we show that North Afar has the most pronounced Afar Plume signature of all the Afar volcanism. This suggests that compositional variations during rift evolution do not always reflect a progressive transition toward a MORB-like composition. Instead, an increasing influence of a plume-like component can take place during the formation of the magmatic segments even at the most advanced stage of continental breakup (i.e., North Afar).

Methods

Dataset selection and aim

The dataset is composed of geochemical data from analysis of 1017 samples (Fig. 1) extracted from scientific publications and the open-access petrological databases GEOROC (https://georoc.mpch-mainz.gwdg.de//georoc/; Supplementary text and Supplementary Table S1). The dataset spatially covers all the Series across the entire on-land Afar depression, including the currently active magmatic segments. The dataset spans the period following the Ethiopian-Yemen Flood Basalt eruption (i.e., ~ 29 Ma) to the present. However, the majority of it encompasses the Stratoid, Gulf and Axial Series and therefore since ~ 5 Ma[35]. Based on the available dataset we perform three cluster analysis tests.

For the first test we carried out the cluster analysis of all the 1017 samples using all major elements (SiO_2, TiO_2, Al_2O_3, FeO_{tot}, CaO, MgO, MnO, K_2O, Na_2O, P_2O_5) normalized to 100% on anhydrous basis as input features (Supplementary Table S1). This test aims to investigate the main differentiation process (i.e., fractional crystallisation) of Afar volcanism, while assessing whether other magmatic processes (e.g., magma mixing, crustal assimilation) that likely affect only a subset of the samples can be identified by cluster analysis.

For the second test we carried out the cluster analysis using a selection of trace elements (Dy/Yb, Zr/Y, La/Sm, Th/Ta, Zr/Nb, Zr/Hf, and Th) as input features (Supplementary Table S1). The trace element data are available for 287 samples. This test aims to investigate variations in the primitive melts, possibly related to changes in depth of melting (Dy/Yb), degree of partial melting (La/Sm) or involved mantle reservoirs (Zr/Hf, Zr/Y, Th/Ta and Zr/Nb). Th has been inserted to keep track of the melt's evolution degree. For test 2, we carried out three separate cluster analyses on the same sample dataset, each with different input element ratios. This approach was implemented to assess the outcome of the cluster analysis when using different combinations of ratios. Particular focus was put on minimizing the effect of using redundant correlated ratios as input features (detailed explanation at section *Test 2 - Trace element ratios*). The goodness of the results was evaluated by checking the correspondence of the clusters with well-defined spatio-temporal regions of Afar (e.g., volcanoes, rift segments, volcanic formations; Supplementary Table S1).

For the third test we carried out the cluster analysis of 144 samples using isotopic ratios (^{143}Nd/^{144}Nd, ^{87}Sr/^{86}Sr, ^{206}Pb/^{204}Pb, ^{207}Pb/^{204}Pb, ^{208}Pb/^{204}Pb) as input features (Supplementary text and Supplementary Table S1). This test aims to investigate the mantle reservoirs involved in the partial melting.

Clustering algorithms

Clustering methods are widely used to subdivide the multivariate observations selected for the three tests (i.e., samples) into representative groups[36–38]. In this work we used two clustering algorithms, hierarchical and K-means, both widely used in Earth science applications to identify similar groups[21–24]. The hierarchical cluster algorithm starts by considering all data points as individual clusters and step-by-step merging the closest clusters into larger groups based on their measured Euclidean distance[39]. In contrast, K-means clustering first computes *k* initial cluster centroids, called seeds. Then, it iteratively assigns each point to the nearest cluster centroid and recomputes the cluster centroid positions, until no significant changes for the assignment of the points to the cluster centroids occur[40].

We standardized the dataset using the z-scores method to prevent variables with different units and different data ranges from skewing the clustering results[41]. This standardization procedure calculated using the formula z = (x - μ) / σ, transforms each raw concentration (x) into a z-score (z) by subtracting the population mean (μ) and dividing by the population standard deviation (σ). The cluster analysis was then performed using the standardized data. For test 1, since the major elements are constrained by their constant-sum (i.e., they total 100%), we also performed cluster analysis on the standardized dataset after applying centred log-ratio (clr), additive log-ratio (alr), and isometric log-ratio (ilr) transformation. These results are presented in the supplementary text.

We used the Julia implementation of the two cluster analysis algorithms available in the Clustering Julia package (*juliastats.org/Clustering.jl/*). We assumed a number of clusters, k, ranging from 2 to 10, and did not extend the range further, as the optimal k consistently fell well below this upper limit. For the K-means algorithm, for each value of *k*, we executed 1 time the algorithm for a maximum of 1000 iterations starting from the set of seeds computed by the method proposed by Arthur and Vassilvitskii[40] and we then executed 10,000 times the algorithm for a maximum of 1000 iterations starting from a set of random seeds. At the end, we reported the clustering with the minimum cost.

Selection of the representative number of clusters

Cluster analysis does not identify the best number of clusters, k. While several quantitative indicators of the best number of clusters exist such as Silhouette, Krzanowski-Lai, Calinski-Harabasz, it remains unclear which is the most reliable, as they are not always consistent[42,43]. Furthermore, these indicators struggle with common data challenges, such as variations in cluster density, skewed distributions or the presence of subclusters[44] and they are not sufficient on their own to evaluate the cluster validity for a geochemical dataset[38]. In fact, they often favour a low number of clusters as the optimal solution or produce inconsistent results across different methods[42,45] (Supplementary Table S2).

Instead in this work we take the approach of using two different cluster analysis algorithms, hierarchical (*h*) and K-means (*k*) and finding the best number of clusters, k, where the algorithms predictions of k are most similar. In order to evaluate the similarity between the two predictions, we used the Dice Similarity Coefficient (DSC) defined by Dice[46]. This coefficient is equal to $2a/(2a + b + c)$, where a is the number of pairs of observations which are in the same cluster in both h and k clusters, b is the number of pairs of observations which are in the same clusters as predicted by k but not in the same cluster as predicted by h, and c is the number of pairs of observations which are in the same clusters as predicted by h but not in the same cluster as predicted by k. The DSC ranges between 0, when two sets have no elements in common, to 1, when two sets are identical. For each test we select the best number of cluster configurations (BCC) by selecting the highest number of clusters having a DSC greater than 0.8 (Supplementary Table S2).

To test the results of our cluster analysis, we also applied principal component analysis (PCA) on the standardized dataset. PCA is a dimensionality reduction technique that facilitates the interpretation of complex multivariate data while minimizing information loss. In this context, PCA was used to assess the goodness of the identified clusters by evaluating how well they separate across the input features, with the results shown in Figs. 2, 3 and 4.

Results

Test 1 - Major elements

The BCC identifies 7 clusters for test 1 (labelled CL1.1 to CL1.7), which will be presented here using the hierarchical clustering median values of their input features. Nearly all the clusters are distinct based on their degree of evolution, characterized by increasing SiO_2, K_2O, and Na_2O, alongside decreasing MgO, CaO, and Al_2O_3. Meanwhile, TiO_2, FeO_{tot}, and P_2O_5 initially increase and start to decrease at mid-evolved terms (i.e., MgO 4–5 wt%) with similar patterns found by hierarchical and K-means (Supplementary Figs. S1 and S2). However, two silicic clusters are distinguished (CL1.5 and CL1.6, SiO_2 72.54 wt% and 72.64 wt% respectively) with CL1.6 located mainly at Dabbahu, Badi and at Nabro volcanoes, showing higher FeO_{tot} and MnO (respectively 6.09 wt% and 0.21 wt%) for the same SiO_2 with respect to CL1.5 (respectively 3.59 wt% and 0.11 wt%) (Fig. 2). Furthermore, CL1.7 groups together samples located at the Asal magmatic segment having higher Al_2O_3 and lower FeO (respectively 22.05 wt% and 6.75 wt%) with respect to the other mafic samples (e.g., CL1.1, Al_2O_3 15.75 wt% and FeO 11.16 wt%) (Fig. 2; Supplementary Fig. S1). The test 1 cluster analysis was performed on the standardized dataset, and on the standardized dataset after applying log-ratio transformation (supplementary text). The two sets of results are broadly consistent. However, the log-ratio transformed dataset provides less clear results (see supplementary text), so we prefer the solution obtained without the transformation.

Test 2 - Trace element ratios

We carried out three separate cluster analyses using the same dataset but different input element ratios. Using the first set of features (Supplementary Table S1; Dy/Yb, Zr/Y, La/Sm, La/Yb, Th/Ta, Th/Zr, Zr/Nb, Nb/Ta, Zr/Hf and K/Th), the DSC indicated 2 as the BCC. However, this result lacks a clear distinction between evolved and mafic samples (Supplementary Figs. S3A and S4A). We therefore perform a new test (Supplementary Table S1) substituting the feature K/Th with Th to keep track of the degree of magma evolution, preventing mafic and felsic samples to be clustered together. This test yielded a BCC with cluster 4 and 10 both exhibiting the same DSC (Supplementary Figs. S3B and S4B). However, given the similar geochemical behaviour shared by groups of elements having similar characteristics (e.g., LREE, HFSE), correlation between trace element ratios can occur and influence the clustering results. We therefore evaluated the correlation among the input features by means of Pearson correlation coefficient and removed redundant trace element ratios (i.e., La/Yb, Th/Zr and Nb/Ta; Supplementary Table S1). By significantly reducing correlated features and using only the non-redundant features configuration (i.e., Dy/Yb, Zr/Y, La/Sm, Th/Ta, Zr/Nb, Zr/Hf, and Th) we found a BCC of 7 clusters

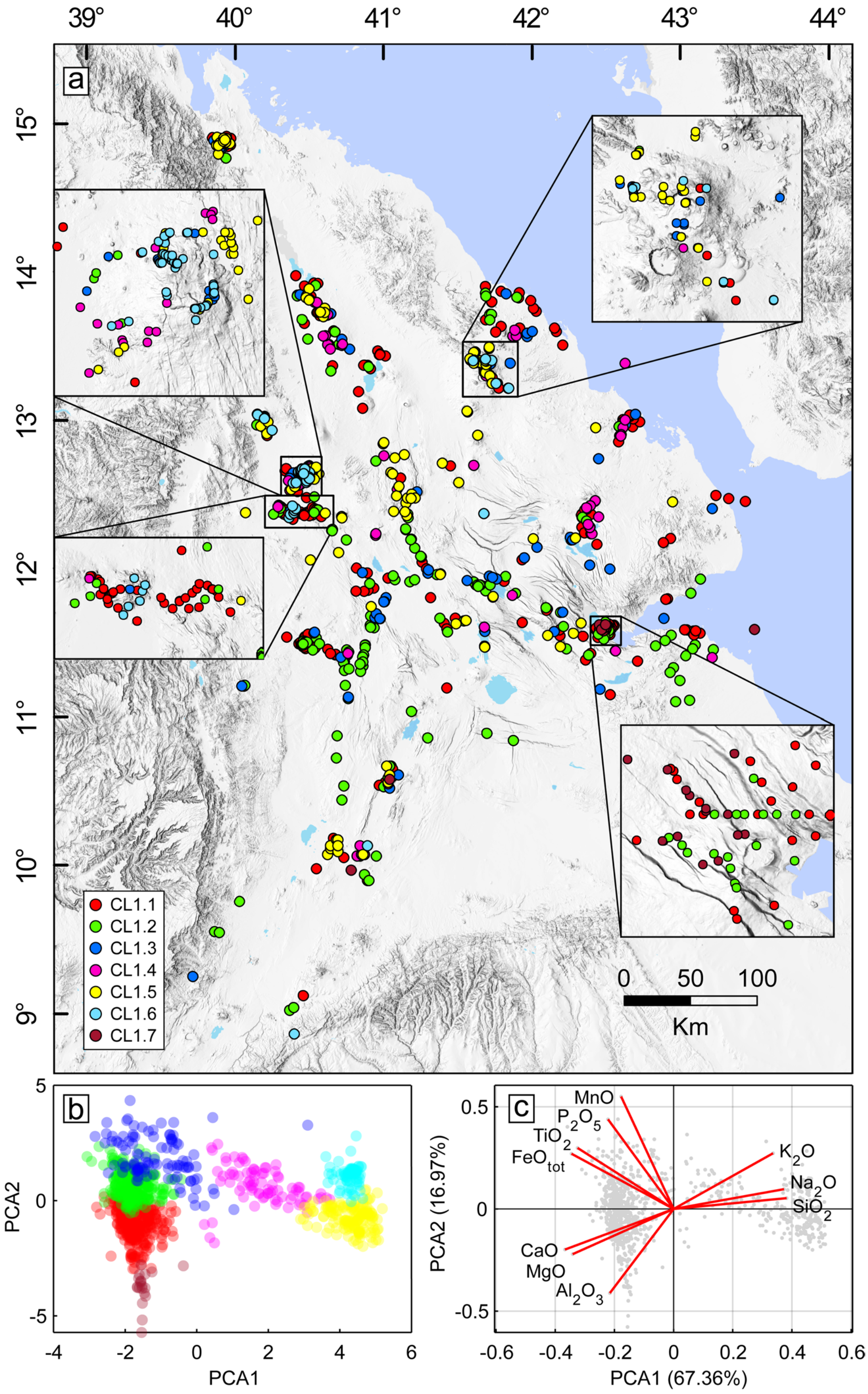

Fig. 2. Samples distribution and principal component analysis (PCA) of test 1 hierarchical clustering BCC. Geographic distribution of the samples used in test 1 (**a**) and PCA plot showing sample scores of the first two principal components (**b**; PCA1 and PCA2), with samples colored according to their cluster number (7 clusters identified by BCC). (**c**) Contribution of each variable to the first two principal components, represented by loading vectors (red lines). The percentage of total variance explained by PCA1 and PCA2 is indicated in parentheses. The corresponding K-means clustering results are provided in Supplementary Figs. S1 and S2 for comparison. This figure was created using ArcGIS Pro 3.4.0 (https://www.esri.com/en-us/home) by combining the Terrain - Multi-Directional Hillshade and World Water Bodies layers.

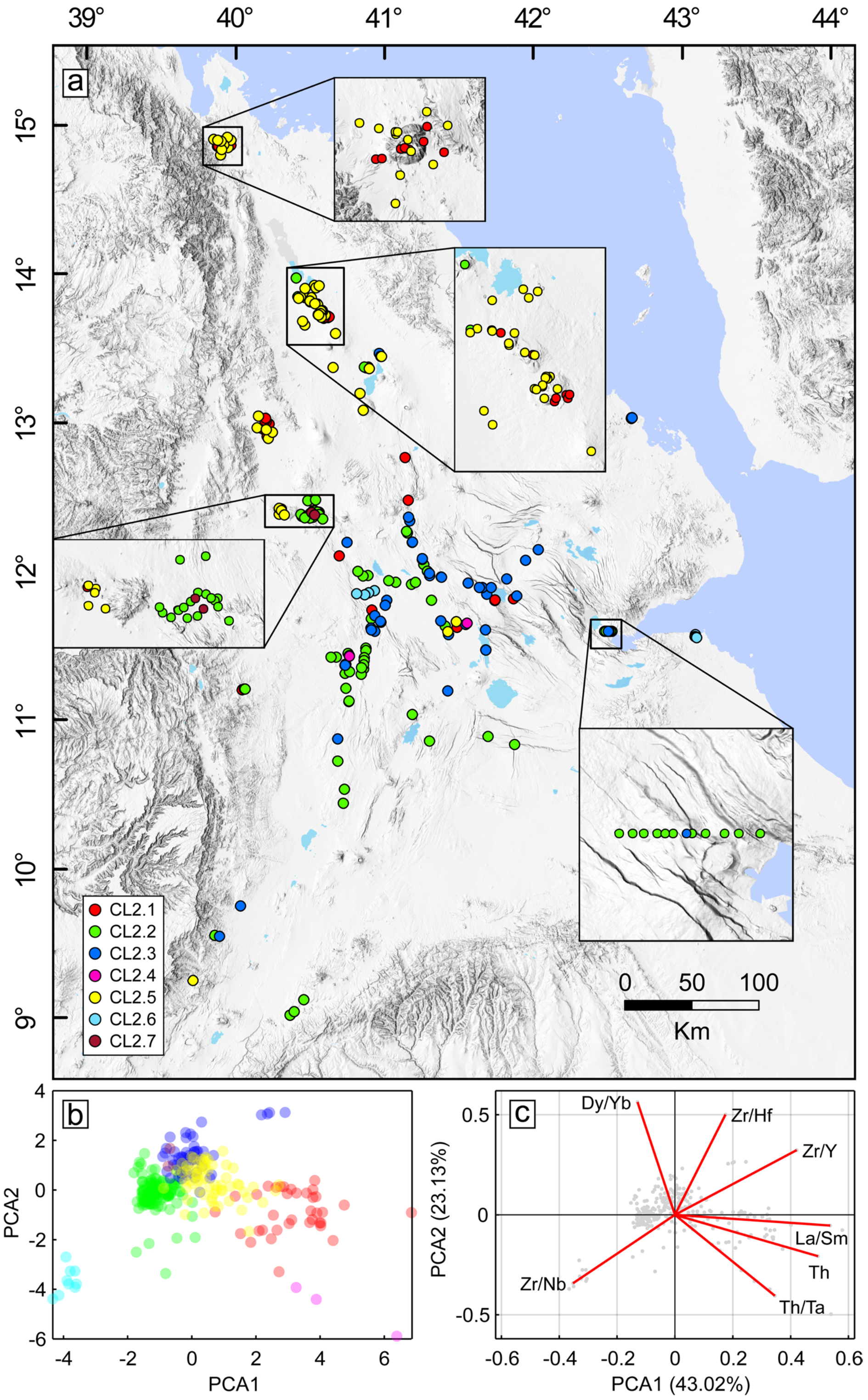

Fig. 3. Samples distribution and principal component analysis (PCA) of test 2 hierarchical clustering BCC. Geographic distribution of the samples used in test 2 (**a**) and PCA plot showing sample scores of the first two principal components (**b**; PCA1 and PCA2), with samples colored according to their cluster number (7 clusters identified by BCC). (**c**) Contribution of each variable to the first two principal components, represented by loading vectors (red lines). The percentage of total variance explained by PCA1 and PCA2 is indicated in parentheses. The corresponding K-means clustering results are provided in Supplementary Figs. S3 and S4 for comparison. This figure was created using ArcGIS Pro 3.4.0 (https://www.esri.com/en-us/home) by combining the Terrain - Multi-Directional Hillshade and World Water Bodies layers.

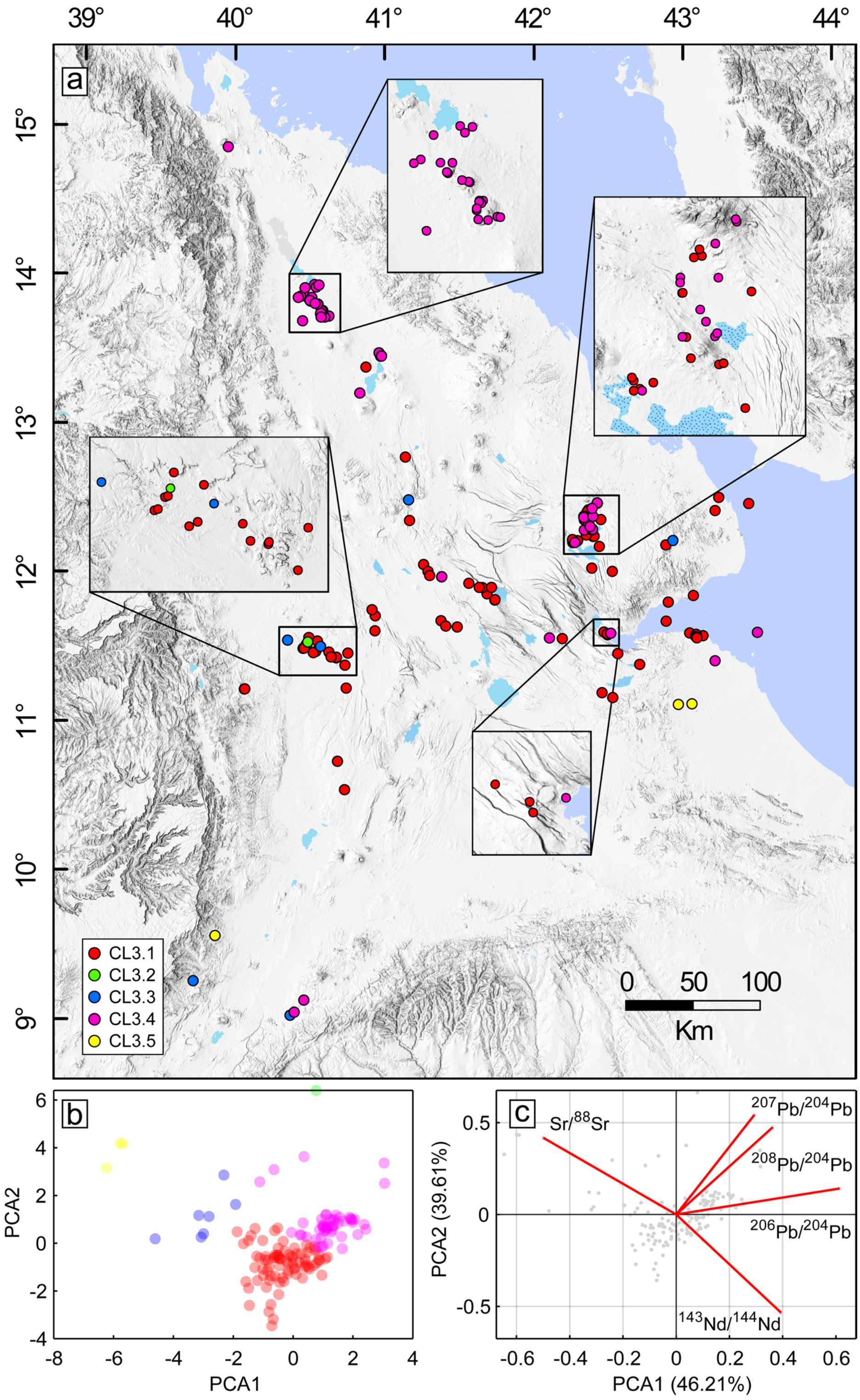

Fig. 4. Samples distribution and principal component analysis (PCA) of test 3 hierarchical clustering BCC. Geographic distribution of the samples used in test 3 (**a**) and PCA plot showing sample scores of the first two principal components (**b**; PCA1 and PCA2), with samples colored according to their cluster number (5 clusters identified by BCC). (**c**) Contribution of each variable to the first two principal components, represented by loading vectors (red lines). The percentage of total variance explained by PCA1 and PCA2 is indicated in parentheses. The corresponding K-means clustering results are provided in Supplementary Figs. S5 and S6 for comparison. This figure was created using ArcGIS Pro 3.4.0 (https://www.esri.com/en-us/home) by combining the Terrain - Multi-Directional Hillshade and World Water Bodies layers.

(labelled CL2.1 to CL2.7), which will be presented here using the hierarchical clustering median values of their input features. We identify a cluster with the highest Th (14.22 ppm), grouping together the evolved samples throughout Afar (CL2.1; Fig. 3; Supplementary Figs. S3C and S4C). CL2.6 identifies a small subset of samples located at the Hayyabley Volcano (Djibouti) and at Manda Hararo magmatic segment, having the lowest Th (0.22 ppm), Zr/Y (2.09), La/Sm (1.30) and the highest Zr/Nb (18.1). CL2.4 groups together a few samples located in the Tendaho and Mile areas, having the highest Th/Ta (5.83; Fig. 3; Supplementary Fig. S3C). CL2.7 groups two samples with distinctively high Zr/Hf (57.1) and low Dy/Yb (1.53; Fig. 3; Supplementary Fig. S3C). The remaining three clusters (CL2.5, CL2.3 and CL2.2) represent most of the mafic samples in the dataset. Among these 3 clusters CL2.5 have the higher La/Sm (4.17) and lowest Zr/Nb (5.16) and are nearly all located in North Afar (at Erta Ale, Alid, Ma'Alalta and Durrie). The samples of the other two clusters are all located in Central and Southern Afar with CL2.3 overall grouping together the US samples and showing more distinctly elevated Zr/Y (6.87) and Dy/Yb (2.32) and moderately higher La/Sm (3.41) and Zr/Hf (41.83) with respect to the LS and the Axial samples of Tendaho-Manda Hararo and Asal, grouped together in CL2.2 (La/Sm 2.81, Zr/Y 5.22, Zr/Hf 39.43 and Dy/Yb 2.07) (Fig. 3; Supplementary Fig. S3C).

Test 3 – Isotopic ratios

The BCC identifies 5 clusters for test 3 (labelled CL3.1 to CL3.5), which will be presented here using the hierarchical clustering median values of their input features. CL3.2 clustered only one sample due to its high $^{208}Pb/^{204}Pb$ (41.46; Fig. 4). CL3.5 and CL3.3 have similar lower $^{143}Nd/^{144}Nd$ (respectively 0.51258 and 0.51279) and higher $^{87}Sr/^{86}Sr$ (respectively 0.70574 and 0.70455) with respect to the other samples (e.g., CL3.1, $^{143}Nd/^{144}Nd$ 0.51292 and $^{87}Sr/^{86}Sr$ 0.70363; Fig. 4; Supplementary Figs. S5 and S6). CL3.5 and CL3.3 are also among the samples with the lower $^{206}Pb/^{204}Pb$ (respectively 17.88 and 18.41). The rest of the samples are distinct in two main groups (CL3.4 and CL3.1) based on the Pb isotopic ratios. CL3.4 group together all the samples of Northern Afar and part of the samples from the Manda Inakir magmatic segment, having higher $^{206}Pb/^{204}Pb$ (19.10), $^{207}Pb/^{204}Pb$ (15.6) and $^{208}Pb/^{204}Pb$ (39.1) with respect to the rest of the samples from Central and Southern Afar grouped together in CL3.1 ($^{206}Pb/^{204}Pb$ 18.62, $^{207}Pb/^{204}Pb$ 15.56 and $^{208}Pb/^{204}Pb$ 38.78) (Fig. 4; Supplementary Figs. S5 and S6).

Discussion

By using cluster analysis we identified groups of samples with chemical similarities (i.e., clusters) corresponding to well-defined spatio-temporal regions of Afar (e.g., volcanoes, rift segments, volcanic formations). We show that using a non-redundant geochemical dataset is key to obtaining reliable and interpretable clusters. We also suggest that using the DSC to compare hierarchical and K-means clustering algorithms ensures reliable selection of the number of groups required to divide a geochemical dataset. Our results of test 1 correspond to groups previously identified in the literature (see discussion in section *Magmatic differentiation*), confirming the efficiency of automated cluster analysis applied to geochemical data. In this section we investigated magma differentiation by means of test 1 (section *Magmatic differentiation*) and magma source by means of test 2 and 3 (section *Afar mantle source*).

Magmatic differentiation

Overall, the Afar magmatic differentiation is mainly controlled by fractional crystallisation of olivine, pyroxene, plagioclase, Fe-Ti oxide and apatite[28,47,48]. The major elements of the whole 1017 samples of test 1 (SiO_2, TiO_2, AL_2O_3, FeO_{tot}, CAO, MgO, MnO, K_2O, Na_2O, P_2O_5) are grouped mainly accordingly to their degree of evolution (CL1.1, CL1.2, CL1.3, CL1.4 and CL1.5; Fig. 2; Supplementary Figs. S1 and S2). However, clusters outside the main fractional crystallisation path are identified. We identified a group of samples previously recognized in the literature and characterised by plagioclase accumulation[49] (CL1.7 Fig. 2; Supplementary Figs. S1 and S2). Beside plagioclase accumulation being quite diffuse in the recent magmatic activity of the Asal magmatic segment[49] the cluster analysis did not identify this process for any other segment. Furthermore, the pantellerite group of peralkaline rocks previously described in the literature by Hutchison et al.[2] have been identified with clustering (CL1.6; Fig. 2; Supplementary Figs. S1 and S2). These observations indicate that cluster analysis successfully identifies distinct magmatic characteristics even outside the main fractional crystallisation process.

Afar mantle source

Both test 2 (Dy/Yb, Zr/Y, La/Sm, Th/Ta, Zr/Nb, Zr/Hf, and Th) and test 3 ($^{143}Nd/^{144}Nd$, $^{87}Sr/^{86}Sr$, $^{206}Pb/^{204}Pb$, $^{207}Pb/^{204}Pb$, $^{208}Pb/^{204}Pb$) cluster analysis have been used to assess variation in the Afar mantle source. Clustering of the trace elements distinguished the volcanism of Central-Southern Afar in two groups (i.e., CL2.2 and CL2.3) mainly due to Dy/Yb and Zr/Y variations (Fig. 5A; Supplementary Figs. S3C and S4C). At the same time, the volcanic activity of Northern Afar is distinct from the rest of Afar. The North Afar samples are grouped based on their high $(La/Sm)_N$ and low Zr/Nb (i.e., CL2.5; Fig. 5B) but also according to their high Pb isotopic values, which further links them to some Manda-Inakir samples (CL3.4) and distinguish them from the samples from the rest of Afar (CL3.1; Fig. 4; Supplementary Figs. S5 and S6). Smaller clusters have also been identified, including previously recognized groups such as the LREE-depleted basalt[50,51] (CL2.6) and samples from the Woranso-Mille region[26,28] (CL2.4). However, these groups, along with crustal-contaminated samples (CL3.5 and CL3.3; Supplementary text) and outlier samples (CL2.7 and CL3.2), are not discussed here due to their limited spatial distribution in Afar relative to the regional-scale extent of the other clusters (Supplementary Figs. S7, S8 and S9).

In order to evaluate variations in the mantle source we first evaluated and excluded the effects of crustal contamination and fractional crystallization (Supplementary text). We then examined the results of cluster analysis of the trace elements (test 2) to assess the Afar magma source mineralogy and the results of clustering

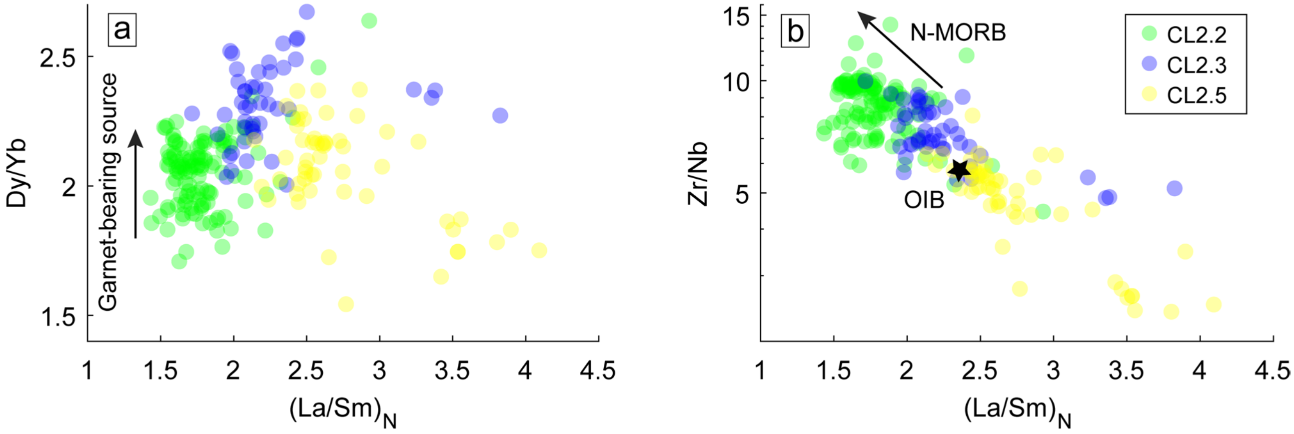

Fig. 5. Partial melting depth and primitive magma signature. Binary trace element ratio plots of the principal clusters mafic lavas (MgO > 4 wt%) of test 2 hierarchical clustering. The samples are colored according to their cluster number. Dy/Yb vs. La_N/Sm_N shows the variations in the melting depth (**a**) while Zr/Nb vs. La_N/Sm_N highlights differences in mantle enrichment (**b**) among Afar lavas. OIB and N-MORB reference values are from Sun and McDonough[71]. Normalizing values after McDonough and Sun[72]. Results including all clusters are shown in Supplementary Fig. S7.

of the isotopes (test 3) to evaluate the interplay between the mantle reservoirs (i.e., AP, PAL and DMM) and the influence of metasomatized lithosphere.

Source mineralogy

To evaluate the partial melting of garnet- or spinel-bearing mantle source and amphibole- and clinopyroxene-bearing metasome we used the results of the trace element clustering and plotted Dy/Yb to track variations in the HREE, versus Dy/Dy* to track variations in the MREE[52] (Fig. 6). Dy* (i.e., $(La_N^{4/13})*(Yb_N^{9/13})$) represent the interpolation between LREE (i.e., La) and HREE (i.e., Yb) and, when compared with the measured Dy value (i.e., $Dy/Dy^* = Dy_N/((La_N^{4/13})*(Yb_N^{9/13}))$), is indicative of MREE depletion or enrichment[52]. Garnet is a HREE-bearing mineral and its presence as a residual phase in the source will lead to a modification of the sole Dy/Yb ratios (Fig. 6). Amphibole preferentially incorporates MREE over HREE (Kd MREE/HREE > 1), while clinopyroxene shows either a similar affinity for both MREE and HREE (Kd MREE/HREE ~ 1) or preference for MREE (i.e., Kd MREE/HREE > 1) depending on the chosen partition coefficient[52,53]. Considering the Dy and Yb Kd variability in clinopyroxene and amphibole, variations in either Dy/Dy* alone or in both Dy/Dy* and Dy/Yb can be therefore attributed to the presence of residual amphibole and/or clinopyroxene in the mantle source (Fig. 6).

All three clusters show well defined and correlated Dy/Yb and Dy/Dy* trends (Fig. 6), arguing for variable residual amphibole and/or clinopyroxene in the respective mantle sources. All clusters show a K negative anomaly and a pronounced Ba and Nb enrichments (with respect to U-Th depletions; Supplementary Fig. S10), indicative of lavas derived from amphibole-bearing sources, as also proposed for the Afar volcanism[18,26,28]. The US (CL2.3) have higher Dy/Yb for the same Dy/Dy* with respect to the LS and the Ax of Central Afar (CL2.2), confirming that Dy/Yb variations result from changes in Yb, which reflect different amounts of residual garnet and thus variations in the partial melting depth[28,49]. North Afar (CL2.5) instead defines a trend that extends to lower Dy/Dy* vs. Dy/Yb values with respect to CL2.2 and CL2.3 indicating an increase of residual amphibole and/or clinopyroxene in the North Afar mantle source. Considering the K negative anomaly, the Ba-Nb enrichment (Supplementary Fig. S10) and the diffuse amphibole-bearing metasomatism in Afar[18,26,28], the lower Dy/Dy* vs. Dy/Yb trend could suggest an increase of residual amphibole rather than an increase in clinopyroxene. Modeled partial melts of amphibole metasomatic veins have been shown to closely resemble OIB magmas, in particular, presence of accessory minerals in the model hydrous cumulates (i.e., apatite, allanite, titanite, and zircon) contributes to the high concentrations of incompatible elements[16,17]. The higher partial melting of amphibole-bearing metasomes can therefore explain the North Afar lower Zr/Nb (i.e., CL2.5) with respect to the volcanism across the rest of Afar (Fig. 5).

Isotopic signatures of Afar reservoirs

Overall, the Pb isotope analysis indicate that Afar magmatism arises from a mix between a deep Afar Plume and a shallower mantle composed of varying proportions of depleted mantle reservoir and material linked to the Pan-African lithosphere[9] (Fig. 7). Nearly all Central and Southern Afar samples (CL3.1) are clustered together, suggesting a lack of major variations in the mantle reservoirs during partial melting (Fig. 7). This confirms that the observed trace element variations in Central and Southern Afar (e.g., Dy/Yb; CL2.2 and CL2.3 in Fig. 5A) must be related to changes in the mantle mineralogy driven by variations in the depth of melting[28,49].

All North Afar samples and part of the Manda Inakir samples (CL3.4) have higher $^{206}Pb/^{204}Pb$, $^{207}Pb/^{204}Pb$ and $^{208}Pb/^{204}Pb$ with respect to Central and Southern Afar samples (CL3.1; Fig. 7). In Afar, the source of radiogenic $^{206}Pb/^{204}Pb$ is the Afar Plume[9], arguing for an increase of the AP contribution during partial melting

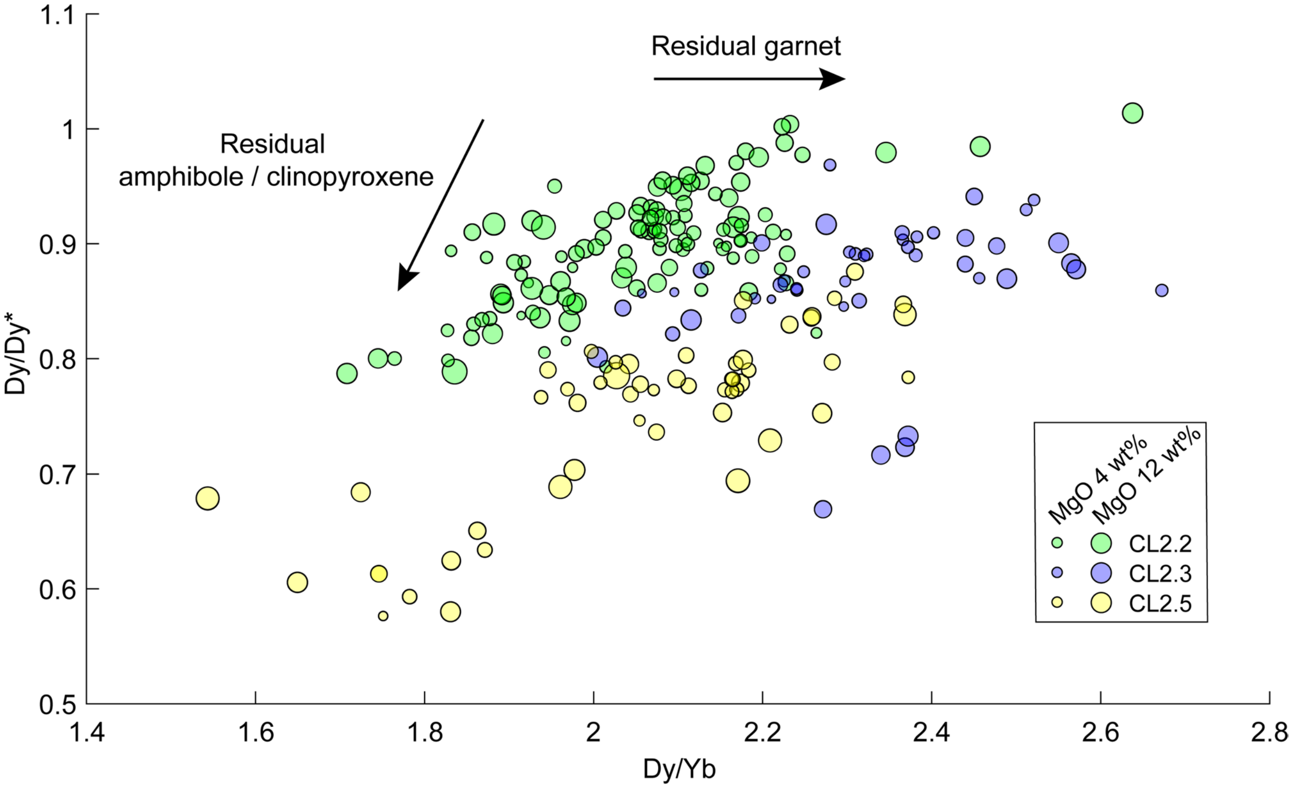

Fig. 6. Metasomatism of the lithosphere. Dy/Dy* vs. Dy/Yb plot of the principal clusters mafic lavas (MgO > 4 wt%) of test 2 hierarchical clustering, used to assess the influence of residual mantle minerals. The samples are colored according to their cluster number. Vector trends for residual minerals control follow Davidson et al.[52]. Symbol size scaled based on the MgO wt% content. See section *Source mineralogy* for details. Results including all geochemical clusters are shown in Supplementary Fig. S8.

beneath North Afar with respect to the rest of Afar (Fig. 7). Accordingly, the North Afar and Manda Inakir samples (CL3.4) also have a slightly higher $^{207}Pb/^{204}Pb$ and $^{208}Pb/^{204}Pb$ compared to the rest of Afar volcanism (CL3.1). This observation agrees with the Northern Afar low Zr/Nb ratio (CL2.5 in Fig. 5B), which argues for an OIB-like mantle source. Alternatively, the high $^{206}Pb/^{204}Pb$ could also result from enhanced partial melting of a metasomatized lithosphere[17] that retained the isotopic composition of the Afar Plume, which was likely responsible for the metasomatism in Afar[5,18]. However, this scenario is not fully supported by the $^{87}Sr/^{86}Sr$ vs. $^{143}Nd/^{144}Nd$ data, which show no variations between the two clusters. This suggests that the contribution of the lithospheric component (i.e., PAL) during partial melting did not change significantly (Fig. 7), and therefore argues against a major role played by the metasomatized lithosphere in modifying the Pb isotopic composition. We therefore suggest that the observed isotopic variations are likely due to an increased contribution from the AP for North Afar with respect to the Central and Southern Afar.

Implication for rift evolution

This study confirms the change in the depth of partial melting within Central and Southern Afar between the deeper Upper Stratoid (CL2.3; 2.9–0.9 Ma) and the shallower Lower Stratoid (4.9–2.6 Ma) and Axial volcanism (< 0.7 Ma) (CL2.2; Figs. 5 and 6). This observation corroborates previous findings suggesting a major change in rift setting between Lower and Upper Stratoid at ~ 2.6 Ma[28,54], and the subsequent shallowing of the partial melting during the formation of the magmatic segments[28,49] (~ 1 Ma). Furthermore, we provided evidence for an increase of amphibole-bearing metasomes in partial melting beneath Northern Afar (CL2.5; Fig. 6). Lastly, we revealed Northern Afar has lower Zr/Nb (CL2.5 in Fig. 5) and higher $^{206}Pb/^{204}Pb$, $^{207}Pb/^{204}Pb$ and $^{208}Pb/^{204}Pb$ (CL3.4 in Fig. 7) with respect to the rest of Afar volcanism, suggesting an increase of the Afar Plume component.

Based on its volcano-tectonic activity[47,55–57] North Afar is considered the most mature of the Afar magmatic segments, representing the very last stage of continental breakup or even a proto-oceanic spreading phase[55,58–60]. Accordingly, the crust in North Afar is thinner[58,61] (14–16 km) than the rest of the rift[54,61] (broadly 20–30 km). The persistent and voluminous magmatic activity in North Afar resulted in the formation of the Erta Ale magmatic segment, which comprises seven volcanoes and differ from other Quaternary rift segments in Afar. Despite the voluminous magmatic activity, Erta Ale mantle potential temperature[62] (~ 1.458 °C) is similar to the one observed for the rest of Afar[27,31] (1350–1500 C) suggesting that no variation in temperature drove the higher magmatic flux. According to Brounce et al.[62], the initial pressure of Erta Ale partial melting (93 –63 km) requires the presence of fusible mantle components for melting, that could be fed by the Afar Plume material containing

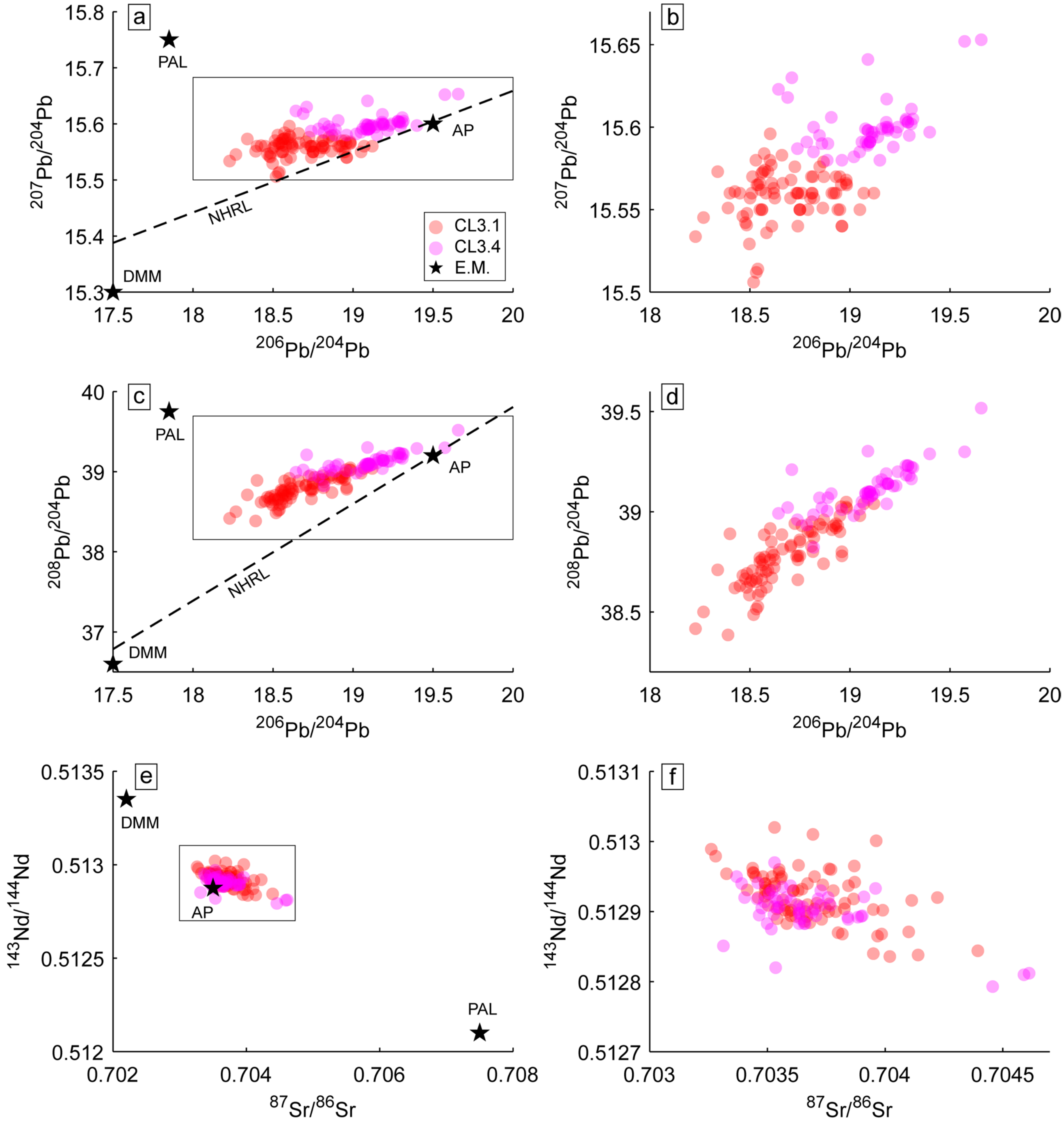

Fig. 7. Mantle reservoirs. Binary isotopic plots of the principal clusters of test 3 hierarchical clustering. (**a**) ^{207}Pb/^{204}Pb vs. ^{206}Pb/^{204}Pb, (**c**) ^{208}Pb/^{204}Pb vs. ^{206}Pb/^{204}Pb, (**e**) ^{87}Sr/^{86}Sr vs. ^{143}Nd/^{144}Nd. On the right side of the figure the zooms of the same isotopic ratios are presented (**b**,**d**,**f**). The black line in (**a**) and (**c**) is the North Hemisphere Reference Line (NHRL) from Hart[73]. DMM (Depleted Morb Mantle), AP (Afar Plume) and PAL (Pan-African Lithosphere) reference values are from Rooney et al.[9]. Results including all geochemical clusters are shown in Supplementary Fig. S9.

higher-than-typical H_2O contents[62] (852 ± 167 ppm) and by the presence of easily-fusible amphibole-bearing metasomes[16,26] (Fig. 6).

Spatio-temporal variations in plume-like signatures can be attributed to the sampling of different sectors of the plume head, either proximal or distal from the plume center[63,64]. While this could be the case for the Manda Inakir samples, which lie relatively close to the inferred Afar plume centre located beneath central Afar[7,9,65], Erta Ale is one of the farthest volcanoes from the proposed plume location, suggesting its plume-like chemistry cannot be related to the distance from the plume. These observations introduce additional complexity to our understanding of the rift mechanism when compared to what is observed for the Ethiopian flood basalt model, where plume activity and the effect of the metasomatized lithosphere decrease systematically away from the plume axis[64,66]. Heterogeneities within the plume[67] or in the associated metasomatized lithosphere[68] can potentially explain the spatio-temporal variations in plume-like contribution observed in this work. However, the fact that these chemical variations were observed only at the most advanced stages of the rift (i.e., Axial volcanism) suggests a strong correlation with the evolution of the rift itself. At the Panarà-Etendeka igneous province, an increase of the plume signature has been observed. The initial Panarà continental flood basalt eruption was primarily influenced by the lithospheric contribution, whereas the subsequent rifting phase was more strongly affected by the sub-lithospheric plume[69]. A similar evolutionary trend has been hypothesized for the Kenyan Rift, where current magmatism is still dominated by lithospheric contributions, and an increasing plume influence is expected in later stages[70]. Beyond the main rift segments of the East African Rift System, magmatic activity occurring on the Ethiopian Plateau shows an increase of the plume contribution after the continental flood basalt eruption[14]. The explanation of these patterns is that an ascending plume can weaken the lithosphere by increasing the geothermal gradient and forming metasome[16,17]. This process, associated with rift stretching, lead to progressive partial melting and thinning the lithosphere[64] as well as lithospheric dripping[66], whereby dense metasomatized lithosphere drips into the asthenosphere and melts during gravitational sinking, further contributing to lithospheric thinning. As a result, the lithospheric signature decreases in favour of the sub-lithospheric plume component[14,69,70]. We suggest that in North Afar, the focusing of the mantle plume into the melt zone beneath the thin lithosphere is the primary reason for increased Afar Plume contribution in the melts. In addition, the results point towards some contribution from partial melting of metasomes in the mantle lithosphere which are likely plume related.

Our work demonstrates that compositional variations during rift evolution do not always reflect a progressive transition toward a MORB-like component. Instead, the magmatic activity leading up to continental breakup may be characterized by an increasing plume composition. Specifically, in agreement with the increasing plume activity observed at broader rift scale[14,69], we demonstrate that this increase can take place during the formation of the localised magmatic segments of the rift and explained by focusing of a mantle plume beneath regions of most lithospheric thinning (i.e., North Afar).

Conclusion

In this work, we performed cluster analysis on major elements (test 1), trace element ratios (test 2) and isotopic ratios (test 3) for the entire Afar rift to evaluate the use of clustering techniques in studying differentiation processes and mantle source variations at rift settings. Cluster analysis proved to be a strong complementary tool to the conventional geochemical approach, providing reliable and geologically meaningful results which can be significantly improved by reducing correlated input features (e.g., test 2).

Clustering of major elements proves the reliability of cluster analysis by grouping samples mainly based on their degree of evolution while identifying groups of samples associated with other magmatic processes (e.g., crystal accumulation) previously identified in literature. By means of trace elements cluster analysis two main groups of samples have been distinguished within Central and Southern Afar (test 2; e.g., Dy/Yb, Zr/Y) revealing the deepening of the partial melting column between Lower and Upper Stratoid at ~ 2.6 Ma, and the subsequent shallower partial melting taking place during the formation of the magmatic segments (~ 1 Ma). The samples of North Afar were instead grouped distinctly from the rest of Afar volcanism by cluster analysis of both trace element and isotopic ratios. North Afar activity shows an increase of residual MREE-bearing minerals in the mantle source (i.e., lower Dy/Yb and Dy/Dy*) with respect to the rest of Afar volcanism, which indicate a higher partial melting degree of the amphibole- and/or clinopyroxene-bearing metasomatized lithosphere. Furthermore, North Afar is characterised by the lowest Zr/Nb ratio and by the most radiogenic ^{206}Pb/^{204}Pb, ^{207}Pb/^{204}Pb and ^{208}Pb/^{204}Pb of all Afar volcanism, suggesting an increase of the Afar Plume influence for North Afar volcanism with respect to the rest of Afar.

We showed that compositional variations occurring during rift evolution do not always reflect a progressive transition toward a MORB-like component, instead, an increasing plume-like signature can take place even at the most advanced stage of continental breakup (i.e., North Afar).

Data availability

The complete dataset used in this work and all cluster analysis results are presented in the paper and/or in the Supplementary material.

Received: 25 September 2025; Accepted: 9 January 2026

References

1. Hart, W. K., WoldeGabriel, G., Walter, R. C. & Mertzman, S. A. Basaltic volcanism in ethiopia: constraints on continental rifting and mantle interactions. *J. Geophys. Res. Solid Earth.* **94**, 7731–7748 (1989).
2. Hutchison, W. et al. The evolution of magma during continental rifting: new constraints from the isotopic and trace element signatures of silicic magmas from Ethiopian volcanoes. *Earth Planet. Sci. Lett.* **489**, 203–218 (2018).
3. Rocholl, A., Stein, M., Molzahn, M., Hart, S. R. & Wörner, G. Geochemical evolution of rift magmas by progressive tapping of a stratified mantle source beneath the Ross sea rift, Northern Victoria land, Antarctica. *Earth Planet. Sci. Lett.* **131**, 207–224 (1995).
4. Ayalew, D., Jung, S. & Romer, R. L. Garbe-Schönberg, D. Trace element systematics and Nd, Sr and Pb isotopes of pliocene flood basalt magmas (ethiopian rift): a case for Afar plume-lithosphere interaction. *Chem. Geol.* **493**, 172–188 (2018).
5. Rooney, T. O. The cenozoic magmatism of East africa: part V – magma sources and processes in the East African rift. *Lithos* **360–361**, 105296 (2020).
6. Pearce, J. A. An expert system for the tectonic characterization of ancient volcanic rocks. *J. Volcanol Geotherm. Res.* **32**, 51–65 (1987).

7. Castillo, P. R., Liu, X. & Scarsi, P. The geochemistry and Sr-Nd-Pb isotopic ratios of high 3He/4He Afar and MER basalts indicate a significant role of the African superplume in EARS magmatism. *Lithos* **376–377**, 105791 (2020).
8. Nelson, W. R., Furman, T., van Keken, P. E., Shirey, S. B. & Hanan, B. B. OsHf isotopic insight into mantle plume dynamics beneath the East African rift system. *Chem. Geol.* **320–321**, 66–79 (2012).
9. Rooney, T. O. et al. Upper mantle pollution during Afar plume–continental rift interaction. *J. Petrol.* **53**, 365–389 (2012).
10. Schilling, J., Kingsley, R. H., Hanan, B. B. & McCully, B. L. Nd-Sr-Pb isotopic variations along the Gulf of aden: evidence for Afar mantle Plume-Continental lithosphere interaction. *J. Geophys. Res. Solid Earth*. **97**, 10927–10966 (1992).
11. Watts, E. J., Gernon, T. M., Taylor, R. N., Keir, D. & Pagli, C. Magmatic evolution during proto-oceanic rifting at alu, Dalafilla and Borale volcanoes (afar) determined by trace element and Sr-Nd-Pb isotope geochemistry. *Lithos* **456–457**, 107311 (2023).
12. Rooney, T. O., Mohr, P., Dosso, L. & Hall, C. Geochemical evidence of mantle reservoir evolution during progressive rifting along the Western Afar margin. *Geochim. Cosmochim. Acta*. **102**, 65–88 (2013).
13. Deniel, C., Vidal, P., Coulon, C., Vellutini, P. & Piguet, P. Temporal evolution of mantle sources during continental rifting: the volcanism of Djibouti (afar). *J. Geophys. Res. Solid Earth*. **99**, 2853–2869 (1994).
14. Nelson, W. R. et al. Distinguishing plume and metasomatized lithospheric mantle contributions to post-flood basalt volcanism on the southeastern Ethiopian plateau. *J. Petrol.* **60**, 1063–1094 (2019).
15. Feyissa, D. H., Shinjo, R., Kitagawa, H., Meshesha, D. & Nakamura, E. Petrologic and geochemical characterization of rift-related magmatism at the northernmost main Ethiopian rift: implications for plume-lithosphere interaction and the evolution of rift mantle sources. *Lithos* **282–283**, 240–261 (2017).
16. Pilet, S., Baker, M. B. & Stolper, E. M. Metasomatized lithosphere and the origin of alkaline lavas. *Science* **320**, 916–919 (2008).
17. Pilet, S., Baker, M. B., Müntener, O. & Stolper, E. M. Monte Carlo simulations of metasomatic enrichment in the lithosphere and implications for the source of alkaline basalts. *J. Petrol.* **52**, 1415–1442 (2011).
18. Rooney, T. O., Brown, E. L., Bastow, I. D., Arrowsmith, J. R. & Campisano, C. J. Magmatism during the continent – ocean transition. *Earth Planet. Sci. Lett.* **614**, 118189 (2023).
19. Li, C., Arndt, N. T., Tang, Q. & Ripley, E. M. Trace element indiscrimination diagrams. *Lithos* **232**, 76–83 (2015).
20. Snow, C. A. A Reevaluation of tectonic discrimination diagrams and a new probabilistic approach using large geochemical databases: moving beyond binary and ternary plots. *J Geophys. Res. Solid Earth* **111**, 2005JB003799 (2006).
21. Costa, S. et al. A data driven approach to mineral chemistry unveils magmatic processes associated with long-lasting, low-intensity volcanic activity. *Sci. Rep.* **13**, 1314 (2023).
22. Musu, A. et al. The magmatic evolution of south-east crater (Mt. Etna) during the February–april 2021 sequence of lava fountains from a mineral chemistry perspective. *Bull. Volcanol.* **85**, 33 (2023).
23. Bigdeli, A., Maghsoudi, A. & Ghezelbash, R. Application of self-organizing map (SOM) and K-means clustering algorithms for portraying geochemical anomaly patterns in Moalleman district, NE Iran. *J. Geochem. Explor.* **233**, 106923 (2022).
24. Geranian, H. & Carranza, E. J. M. Mapping of regional-scale multi-element geochemical anomalies using hierarchical clustering algorithms. *Nat. Resour. Res.* **31**, 1841–1865 (2022).
25. Hofmann, C. et al. Timing of the Ethiopian flood basalt event and implications for plume birth and global change. *Nature* **389**, 838–841 (1997).
26. Rooney, T. O. The cenozoic magmatism of East africa: part IV – the terminal stages of rifting preserved in the Northern East African rift system. *Lithos* **360–361**, 105381 (2020).
27. Feyissa, D. H. et al. Transition from plume-driven to plate-driven magmatism in the evolution of the main Ethiopian rift. *J. Petrol.* **60**, 1681–1715 (2019).
28. Tortelli, G. et al. Constraints on the magma source and rift evolution from geochemistry of the stratoid flood basalts (afar, ethiopia). *Geochem. Geophys. Geosyst.* **23**, e2022GC010434 (2022).
29. Lahitte, P., Gillot, P., Kidane, T., Courtillot, V. & Bekele, A. New age constraints on the timing of volcanism in central afar, in the presence of propagating rifts. *J. Geophys. Res. Solid Earth* **108**, 2001JB001689 (2003).
30. Stab, M. et al. Modes of rifting in magma-rich settings: Tectono-magmatic evolution of central Afar. *Tectonics* **35**, 2–38 (2016).
31. Armitage, J. J. et al. Upper mantle temperature and the onset of extension and break-up in Afar, Africa. *Earth Planet. Sci. Lett.* **418**, 78–90 (2015).
32. Hanan, B. B. & Graham, D. W. Lead and helium isotope evidence from oceanic basalts for a common deep source of mantle plumes. *Science* **272**, 991–995 (1996).
33. Rooney, T. O., Nelson, W. R., Dosso, L., Furman, T. & Hanan, B. The role of continental lithosphere metasomes in the production of HIMU-like magmatism on the Northeast African and Arabian plates. *Geology* **42**, 419–422 (2014).
34. White, W. M. Sources of oceanic basalts: radiogenic isotopic evidence. *Geology* **13**, 115–118 (1985).
35. Tortelli, G. et al. Volcanism records plate thinning driven rift localization in Afar (Ethiopia) since 2-2.5 million years ago. *Commun. Earth Environ.* **6**, 395 (2025).
36. Ezugwu, A. E. et al. Automatic clustering algorithms: a systematic review and bibliometric analysis of relevant literature. *Neural Comput. Appl.* **33**, 6247–6306 (2021).
37. Oyewole, G. J. & Thopil, G. A. Data clustering: application and trends. *Artif. Intell. Rev.* **56**, 6439–6475 (2023).
38. Templ, M., Filzmoser, P. & Reimann, C. Cluster analysis applied to regional geochemical data: problems and possibilities. *Appl. Geochem.* **23**, 2198–2213 (2008).
39. Jain, A. K. & Dubes, R. C. *Algorithms for Clustering Data* (Prentice-Hall, Inc., 1988).
40. Arthur, D. & Vassilvitskii, S. k-means++: The advantages of careful seeding. in *Proceedings of the eighteenth annual ACM-SIAM symposium on Discrete algorithms* 1027–1035 (Society for Industrial and Applied Mathematics, 2007).
41. James, G., Witten, D., Hastie, T., Tibshirani, R. & Taylor, J. *An Introduction To Statistical Learning: with Applications in Python* (Springer International Publishing, 2023).
42. Gagolewski, M., Bartoszuk, M. & Cena, A. Are cluster validity measures (in) valid? *Inf. Sci.* **581**, 620–636 (2021).
43. Yerbury, L. W., Campello, R. J. G. B., Livingston, G. C. Jr., Goldsworthy, M. & O'Neil, L. On the use of relative validity indices for comparing clustering approaches. *ACM Trans. Knowl. Discov Data*. **19** (1-144), 53 (2025).
44. Liu, Y., Li, Z., Xiong, H., Gao, X. & Wu, J. Understanding of internal clustering validation measures. in. *IEEE International Conference on Data Mining* 911–916 (IEEE, Sydney, Australia, 2010). (2010).
45. Baarsch, J. & Celebi, M. E. Investigation of internal validity measures for K-means clustering (2012).
46. Dice, L. R. Measures of the amount of Ecologic association between species. *Ecology* **26**, 297–302 (1945).
47. Watts, E. J. et al. Evolution of the alu-dalafilla and Borale volcanoes, afar, Ethiopia. *J. Volcanol Geotherm. Res.* **408**, 107094 (2020).
48. Field, L., Blundy, J., Calvert, A. & Yirgu, G. Magmatic history of dabbahu, a composite volcano in the Afar rift, Ethiopia. *Geol. Soc. Am. Bull.* **125**, 128–147 (2013).
49. Pinzuti, P., Humler, E., Manighetti, I. & Gaudemer, Y. Petrological constraints on melt generation beneath the Asal rift (djibouti) using quaternary basalts. *Geochem. Geophys. Geosyst.* **14**, 2932–2953 (2013).
50. Barrat, J. A. et al. Geochemistry of basalts from Manda Hararo, ethiopia: LREE-depleted basalts in central Afar. *Lithos* **69**, 1–13 (2003).
51. Daoud, M. A. et al. A LREE-depleted component in the Afar plume: further evidence from quaternary Djibouti basalts. *Lithos* **114**, 327–336 (2010).
52. Davidson, J., Turner, S. & Plank, T. Dy/Dy*: variations arising from mantle sources and petrogenetic processes. *J. Petrol.* **54**, 525–537 (2013).

53. Blundy, J. D., Robinson, J. A. C. & Wood, B. J. Heavy REE are compatible in clinopyroxene on the spinel lherzolite solidus. *Earth Planet. Sci. Lett.* **160**, 493–504 (1998).
54. Hammond, J. O. S. et al. The nature of the crust beneath the Afar triple junction: evidence from receiver functions. *Geochem Geophys. Geosystems* **12** (2011).
55. Hurman, G. L. et al. Quantitative analysis of faulting in the Danakil depression rift of afar: the importance of faulting in the final stages of magma-rich rifting. *Tectonics* **42**, e2022TC007607 (2023).
56. Pagli, C. et al. Shallow axial magma chamber at the slow-spreading Erta ale ridge. *Nat. Geosci.* **5**, 284–288 (2012).
57. Rime, V., Foubert, A., Ruch, J. & Kidane, T. Tectonostratigraphic evolution and significance of the Afar depression. *Earth-Sci. Rev.* **244**, 104519 (2023).
58. Bastow, I. D. & Keir, D. The protracted development of the continent–ocean transition in Afar. *Nat. Geosci.* **4**, 248–250 (2011).
59. Keir, D., Bastow, I. D., Pagli, C. & Chambers, E. L. The development of extension and magmatism in the red sea rift of Afar. *Tectonophysics* **607**, 98–114 (2013).
60. Le Gall, B. et al. The red beds series in the Erta ale segment, North afar. Evidence for a 6 ma-old post-rift basin prior to continental rupturing. *Tectonophysics* **747–748**, 373–389 (2018).
61. Ahmed, A. et al. Across and along-strike crustal structure variations of the Western Afar margin and adjacent plateau: insights from receiver functions analysis. *J. Afr. Earth Sci.* **192**, 104570 (2022).
62. Brounce, M., Scoggins, S., Fischer, T. P., Ford, H. & Byrnes, J. Volatiles and redox along the east african rift. *Geochem. Geophys. Geosyst.* **25**, e2024GC011657 (2024).
63. Homrighausen, S. et al. Unexpected HIMU-type late-stage volcanism on the Walvis ridge. *Earth Planet. Sci. Lett.* **492**, 251–263 (2018).
64. Beccaluva, L., Bianchini, G., Natali, C. & Siena, F. Continental flood basalts and mantle plumes: a case study of the Northern Ethiopian plateau. *J. Petrol.* **50**, 1377–1403 (2009).
65. Schilling, J. G. Afar mantle plume: rare Earth evidence. *Nat. Phys. Sci.* **242**, 2–5 (1973).
66. Furman, T., Nelson, W. R. & Elkins-Tanton, L. T. Evolution of the East African rift: drip magmatism, lithospheric thinning and mafic volcanism. *Geochim. Cosmochim. Acta.* **185**, 418–434 (2016).
67. Zhou, H. et al. Geochemistry of Etendeka magmatism: Spatial heterogeneity in the tristan-gough plume head. *Earth Planet. Sci. Lett.* **535**, 116123 (2020).
68. Pfänder, J. A. et al. Recurrent local melting of metasomatised lithospheric mantle in response to continental rifting: constraints from basanites and nephelinites/melilitites from SE Germany. *J. Petrol.* **59**, 667–694 (2018).
69. Beccaluva, L., Bianchini, G., Natali, C. & Siena, F. Plume-related paranà-etendeka igneous province: an evolution from plateau to continental rifting and breakup. *Lithos* **362–363**, 105484 (2020).
70. Macdonald, R. Magmatism of the Kenya rift valley: a review. *Trans. R Soc. Edinb. Earth Sci.* **93**, 239–253 (2002).
71. Sun, S. S. & McDonough, W. F. Chemical and isotopic systematics of oceanic basalts: implications for mantle composition and processes. *Geol. Soc. Lond. Spec. Publ.* **42**, 313–345 (1989).
72. McDonough, W. F. & Sun, S. S. The composition of the Earth. *Chem. Geol.* **120**, 223–253 (1995).
73. Hart, S. R. A large-scale isotope anomaly in the Southern hemisphere mantle. *Nature* **309**, 753–757 (1984).

Acknowledgements

We thanks Laurent Geoffroy for handling the manuscript, and the three anonymous reviewers for their constructive comments, which substantially improved the paper's quality.

Author contributions

G.T. Conceptualization, Data curation, Formal analysis, Investigation, Visualization, Writing - original draft; P.C. Methodology, Software, Writing - review and editing; C.P. Conceptualization, Data curation, Funding acquisition, Supervision, Writing - review and editing; A.G. Investigation, Supervision, Writing - review and editing; D.K. Conceptualization, Funding acquisition, Supervision, Writing - review and editing; L.P. Methodology, Writing - review and editing.

Funding

The research is part of the PhD of G. Tortelli, funded by the 2017 PRIN project-protocol MIUR: 2017P9AT72 PE10. G. Tortelli acknowledges support by the Tuscany Regional PhD Course in Earth Sciences. D.K. is partially supported through NERC grant UKRI1277. This study was carried out within the Space It Up project funded by the Italian Space Agency, ASI, and the Ministry of University and Research, MUR, under contract n. 2024-5-E.0 - CUP n. I53D24000060005.

Declarations

Competing interests

The authors declare no competing interests.

Additional information

Supplementary Information The online version contains supplementary material available at https://doi.org/10.1038/s41598-026-35961-0.

Correspondence and requests for materials should be addressed to G.T.